Water Practice & Technology

IWA PUBLISHING

Water Practice & Technology Vol 19 No 8, 2959 doi: 10.2166/wpt.2024.185

Development of δ-Bi_2O_3/Bi_2SiO_5 heterostructures based on biogenic silica for photocatalytic treatment from organic pollutants

Olga D. Arefieva[a,b,*], Marina S. Vasilyeva[a,b], Denis P. Opra[b], Vladimir V. Tkachev[a], Vladimir V. Korochentsev[a,b], Daria H. Shlyk[b] and Aleksandra I. Slavenskaya[a]

[a] Institute of High Technologies and Advanced Materials, Far Eastern Federal University, Vladivostok, Russian Federation
[b] Institute of Chemistry, Far Eastern Branch, Russian Academy of Sciences, Vladivostok, Russian Federation
*Corresponding author. E-mail: arefeva.od@dvfu.ru

ABSTRACT

δ-Bi_2O_3/Bi_2SiO_5 heterostructural photocatalysts with different contents of bismuth in samples (X-Bi-Si, where X = 10-60% Bi_2O_3) were prepared by the facile sol-gel method using bismuth nitrate and biogenic silica from rice husk biomass as precursors. Fourier transform infrared, scanning electron microscopy, X-ray diffraction, energy-dispersive X-ray fluorescence, and UV-Vis light methods were systematically used to characterize the as-obtained materials. Photodegradation of methyl orange in neutral aqueous solutions (pH (6.8)) under UV irradiation was studied to evaluate its photocatalytic activity. Phase composition, morphology, and photocatalytic activity of the samples depended on the content of bismuth oxide in the samples. Maximum degree of methyl orange degradation was 45% for 50-Bi-Si samples containing photoactive δ-Bi2O3 and Bi_2SiO_5 phases.

Key words: biogenic silica, bismuth oxide, bismuth silicate, heterostructures, photocatalysis, rice husk

HIGHLIGHTS

- Photocatalytically active Bi_2O_3/Bi_2SiO_5 heterostructures have been synthesized by the sol–gel method.
- The content of bismuth oxide of δ-Bi_2O_3/Bi_2SiO_5 affects composition, structure, and photocatalytic properties.
- Electrons are the main active species for the degradation of methyl orange, and $^{\bullet}O_2^-$ plays a supporting role.

GRAPHICAL ABSTRACT

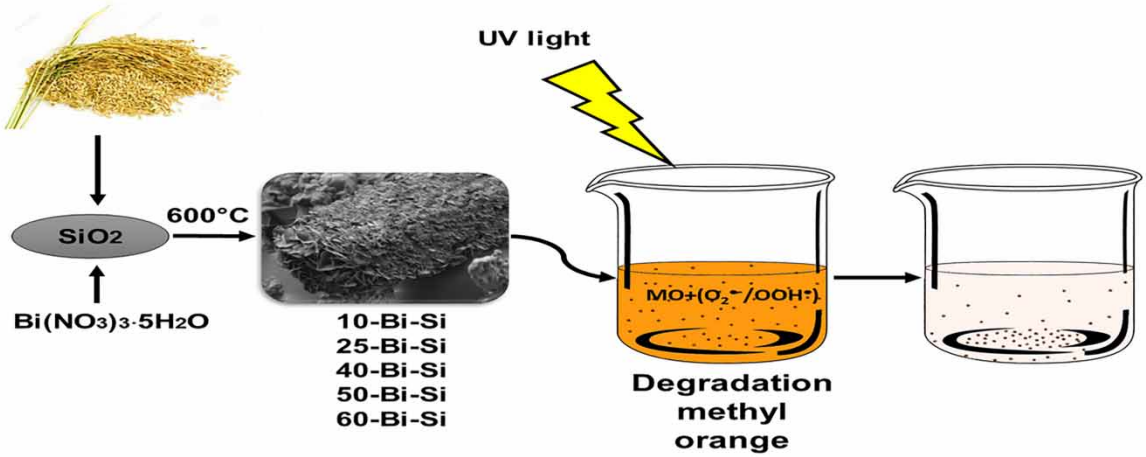

1. INTRODUCTION

The use and management of solid and liquid waste are one of the most important activities of the rice industry nowadays. The reuse of waste makes it possible to achieve a cyclical process and obtain value-added products. In 2019, annual rice production amounted to about 784 million tons, according to the reports of the UN Food and Agriculture Organization (Tyulyagin 2022). Huge amounts of solid waste are generated at various stages of raw rice processing, 20% of which is rice husk that contains ~20% of silica (Pode 2016). This waste can serve as a

source of biogenic amorphous silicon dioxide, which can serve as a basis for developing materials with catalytic properties. However, this application area of biogenic silica is understudied since silica-based supports of catalysts are currently obtained from mineral silicon-containing commercial compounds (Hanna *et al.* 2008; Zhong *et al.* 2011; Bailiche *et al.* 2013; Espro *et al.* 2016; Cui *et al.* 2016).

Fenton-like catalysts and photocatalysts were related to the use of biogenic silica from rice production waste only in a few works (Adam & Andas 2007; Adam *et al.* 2010; Gan & Li 2013; Ghime & Ghosh 2017; Arefieva *et al.* 2021a). Fenton-like iron-containing catalysts based on amorphous silicon dioxide from rice husk were obtained by the sol–gel technique and used in oxalic acid (Ghime & Ghosh 2017), Rhodamine (Gan & Li 2013), and phenol (Adam *et al.* 2010) degradation reactions. Arefieva *et al.* (2021b) showed that Fe-containing Fenton-like catalysts, based on biogenic silica from rice husk obtained by impregnation, could be used to degrade phenol. Arefieva *et al.* (2021b) and Arefieva *et al.* (2020) studied the possibility of using Fenton-like catalysts for the degradation of lignin from alkaline hydrolysates of rice husk by exposure to UV and sunlight irradiation. Photocatalytically active Bi_2O_3/Bi_2SiO_5 oxide heterostructures were obtained by a simple method of $Bi(NO_3)_3$ mechanical stirring and amorphous silicon dioxide from rice husk without using any solvents in the study (Arefieva *et al.* 2021a). The resulting Bi_2O_3/Bi_2SiO_5 heterostructures exhibited photocatalytic activity in the degradation of methyl orange (MO) under sunlight and UV irradiation (Arefieva *et al.* 2021a).

In recent years, photocatalysts based on bismuth(III) compounds have been actively studied due to simple methods of preparation, non-toxicity, and thermal stability. Bismuth(III) oxide forms four crystalline modifications: monoclinic α-Bi_2O_3, tetragonal β-Bi_2O_3, cubic γ-Bi_2O_3, and δ-Bi_2O_3. The band gap for α-Bi_2O_3, β-Bi_2O_3, and δ-Bi_2O_3 is 2.80, 2.48, and 3.01 eV, respectively. According to photocatalytic activity, Bi_2O_3 modifications can be arranged in the following order: β-Bi_2O_3 > α-Bi_2O_3 > δ-Bi_2O_3 (Cheng *et al.* 2010). Bismuth metasilicate (Bi_2SiO_5) and Bi_2O_3/Bi_2SiO_5 heterostructural photocatalysts are promising materials. Such catalysts show high photocatalytic activity during the degradation of various organic pollutants in the sunlight (Zhang *et al.* 2010; Chen *et al.* 2009; Wei *et al.* 2013; Liu *et al.* 2014; Lu *et al.* 2018).

The Bi_2O_3–SiO_2 binary system can include three complex oxide compounds with different Bi/Si atomic ratios, namely bismuth metasilicate Bi_2SiO_5, bismuth orthosilicate $Bi_4Si_3O_{12}$, and sillenite $Bi_{12}SiO_{20}$ (Takamori 1990; Fei *et al.* 2000a, 2000b; Onderka *et al.* 2017). The compounds are arranged in the following order according to the degradation rate of methyl violet under irradiation with visible light: $Bi_2SiO_5 > Bi_4Si_3O_{12} > Bi_{12}SiO_{20}$ (Chen *et al.* 2017). The photocatalytic activity of bismuth silicates depends on the morphology, particle size, and the ratio of the initial components, which, in turn, depend on the method of their synthesis.

Bismuth silicate with various morphologies can be obtained by hydrothermal (Wei *et al.* 2013), solvothermal (Dou *et al.* 2020a), template (Zhang *et al.* 2010; Liu *et al.* 2014; Dou *et al.* 2020b), and sol–gel (Zhang *et al.* 2010; Chen *et al.* 2013; Wu *et al.* 2017) methods. Among all the considered methods, the sol–gel method is the most accessible since it does not require additional equipment. The method is used for the preparation of nano- or submicro-powders (Wu *et al.* 2017) or thin film deposition (Chen *et al.* 2013; Wu *et al.* 2017). For example, Bi_2SiO_5 with nano- and submicro-particles is synthesized by the Pechini sol–gel method (the citrate method; method of polymer complexes) (Wu *et al.* 2017). All studies use commercial silicon-containing compounds. Biogenic silica is not used for synthesizing bismuth silicates. The advantage of biogenic silica is that it is a simple way to obtain its amorphous form, a quick transition from sol to gel with the formation of composites.

The aim of this work is to obtain Bi_2O_3/Bi_2SiO_5 heterostructure photocatalysts from bismuth nitrate and biogenic silica from rice husk using the sol–gel method and study the effect of bismuth and silicon oxide ratios on the composition, structure, and photocatalytic activity in MO degradation reaction of the as-obtained composites.

2. MATERIALS AND METHODS

2.1. Photocatalyst synthesis procedure

In this work, photocatalysts with a theoretical mass content of Bi_2O_3 ranging from 10 to 60% (X-Bi-Si, X = 10–60% Bi_2O_3) were obtained by a procedure proposed by Karthika *et al.* (2019).

The bismuth nitrate pentahydrate $Bi(NO_3)_3{\cdot}5H_2O$ was used as a precursor for the synthesis of Bi_2O_3. This reagent was pre-dried at 60 °C for 2 h, followed by dissolution by heating in a minimum volume of concentrated nitric acid. Minimum volume is required to dissolve a given substance at a given temperature. In the present work, it was determined experimentally.

Biogenic silica (the content of silicon dioxide is ~99%) was obtained from rice husk according to a method described in the study (Zemnukhova *et al.* 2006). The rice husk was obtained in the production of rice of the Dolynny variety of the Far Eastern selection (Ussuriysk, Russia). The husk sample was meshed (~8 mesh) to remove tiny fractions (bran siftings and dust). The raw materials were washed in distilled water, air-dried, and then hydrolyzed by 0.1 M hydrochloric acid by heating to 90 °C within an hour in a laboratory reactor. The temperature was controlled using an EKT Hei Con thermocouple (Heidolph, Germany). The mass ratio of solid to liquid was 1:13. Fibrous residue was filtered through a synthetic fabric filter with a pore size of 15 μm, repeatedly washed with distilled water, and air-dried at $t = 25$ °C for 48 h. Then, oxidative calcination was performed in a WiseTherm muffle furnace (DAIHAN, South Korea) at 600 °C for 3 h. The result was amorphous silicon dioxide in the form of a white powder. This powder was dissolved in a minimal volume of 1 M NaOH solution at 60 °C to obtain a sodium orthosilicate solution.

To form X-Bi-Si samples, the $Bi(NO_3)_3$ dissolved in HNO_3 was added to the sodium orthosilicate solution with constant stirring to pH 6. Masses of the reagents and designations of the photocatalysts are given in Table 1S. Sol was formed while stirring, and this led to a white gel formation during a pH transition. The resulting gel was left to age in a mother liquor for 24 h. The solid precipitate was filtered, washed with distilled water until a neutral reaction, and then dried at 25 °C temperature for 48 h. The resulting powder was calcined in a muffle furnace WiseTherm (DAIHAN, South Korea) to 600 °C for 2.5 h and kept at this temperature for 4 h. The samples were designated depending on the weight content of bismuth oxide in the $Bi(NO_3)_3$–SiO_2 mixture, i.e., the samples containing 10, 25, 40, 50, and 60% were designated as 10-Bi-Si, 25-Bi-Si, 40-Bi-Si, 50-Bi-Si, and 60-Bi-Si, respectively.

2.2. Characterization of the prepared photocatalyst

Elemental analysis of the samples was performed by energy-dispersive X-ray fluorescence (EDXRF) analysis on a Shimadzu EDX 800 HS spectrometer (Japan). IR absorption spectra were recorded within the range of 400–4,000 cm^{-1} in potassium bromide on a Bruker Vertex 70 Fourier-transform spectrometer (Germany) to determine functional groups in the studied samples. X-ray powder diffraction (XRD) analysis of the samples was performed using CuK_α radiation on a Bruker D8 Advance diffractometer (Germany). Morphology and elemental composition of the catalysts' surfaces were studied using the Carl Zeiss Ultra+ scanning electron microscope (SEM) (Germany) equipped with a Thermo Scientific add-on unit from Oxford instruments (England) for energy-dispersive X-ray (EDX) analysis. Optical absorption ability and band gap studies were carried out by ultraviolet–visible diffuse reflectance spectroscopy (DRS) on a Shimadzu UV2600 spectrophotometer (Japan) with wavelengths between 200 and 800 nm using $BaSO_4$ as a reflectance reference. X-ray photoelectron spectra (XPS) were recorded on a Specs ultra-high vacuum photoelectron spectrometer (Germany) with a hemispherical electrostatic analyzer (radius of curvature 150 mm) and a MgK_α radiation source (source energy 1,253.6 eV), along with 10^{-6}–10^{-7} Pa pressures in the analysis chamber. The spectra were processed using the CASA XPS program (CasaXPS Version 2.3.12). The calibration of the electron-binding energy scale was done using an internal standard technique for which C1s level (285.0 eV) was chosen. A spread function of the spectrometer in a mode of characteristic atomic-level registration, which was determined from $Ag3d_{5/2}$ band shape, had 1.2 eV half-width. Survey spectra were obtained with 50 eV pass energy and region spectra with 20 eV pass energy.

Currently, several methods have been proposed for determining the zero-charge point (pH): Frumkin-Atkinson, Zerensen-de Bruin, Parks-Bobyrenko, and Nechiporenko. In this paper, the Zerensen-de Bruin method was used (Noh & Schwarz 1989). The zero-charge point (ZCP) was determined by the following procedure. The studied X-Bi-Si catalysts, where X = 10–60% Bi_2O_3, were sequentially added in small portions (0.05 g) in certain time intervals (5–10 min) into 25 mL of distilled water in a potentiometric cell until constant values of glass electrode potential were reached.

2.3. Procedure for the photocatalytic degradation of MO

Photocatalytic properties of the obtained samples were evaluated by an example of MO degradation (pH 6.8) reaction in the UV spectral region. The concentration of MO was 10 mg L^{-1}. The samples of X-Bi-Si, where X = 10–60% Bi_2O_3, were used as photocatalysts. Individual oxides, Bi_2O_3 and SiO_2 (biogenic silica), were used as control samples. The catalyst dosage was 1 g per 1 L of the MO solution. Photocatalytic decomposition in the UV region was conducted in a 100-mL quartz cell filled with 50 mL of the MO solution (10 mg L^{-1}) and

0.05 g of catalyst. The radiation source was a 100P/F UV lamp (radiation maximum is $\lambda = 365$ nm). The solution was irradiated at constant magnetic stirring (625 rpm) for 3 h.

The absorbance of MO solution was determined by the photocolorimetric method on a UNICO-1201 spectrophotometer by United Products & Instruments (USA) at a wavelength of 460 nm. The degradation degree of MO (χ) was determined by the following formula:

$$\chi = \frac{A_0 - A}{A_0} \times 100\% \quad (1)$$

where A_0 and A are the absorbance of the MO solution before and after photodecomposition, respectively.

The reaction rates are estimated by Equation (2). A commonly used first-order degradation kinetic equation was applied to describe the kinetics of MO degradation by the samples under UV irradiation for 180 min. The kinetic equation is expressed as follows:

$$\ln\left(\frac{C_0}{C}\right) = k_{app}t \quad (2)$$

where C_0 and C (mg L^{-1}) are the initial concentrations of the MO solution and after the reaction, respectively, k_{app} (app – apparent) is the MO degradation rate constant, and t is the reaction time (min). As it is known, solution concentration is related to a value of its absorbance according to the Bouguer–Lambert-Beer law: $A = \varepsilon \times b \times C$, where A, ε, b, and C are the absorbance of a solution, molar absorptivity, path length, and solution concentration, respectively. Therefore, the rate constant (k_{app}) can be determined graphically by the following equation:

$$\ln\left(\frac{A_0}{A}\right) = k_{app}t \quad (3)$$

The Bi content was determined using an atomic absorption spectrophotometer (AAS) SHIMADZU AA-7000 (Japan) equipped with a lamp with a hollow cathode containing bismuth. Conditions for determining bismuth were as follows: wavelength – 223.1 nm; bandwidth – 0.7 nm; lamp current – 10 mA; flame – 15.0 L min^{-1} of air, and 2.2 L min^{-1} of acetylene. All measurements were carried out without background correction. Detection limits of the element range from 0.15 to 20 mg L^{-1}.

2.4. Active species trapping experiment

Several experiments on the degradation of MO in the presence of a photocatalyst 50-Bi-Si were conducted to establish a mechanism of the decomposition process. 2 mmol of isopropanol (IPA), benzoquinone (BQ), hydrogen peroxide (H_2O_2), and ammonium oxalate ($(NH_4)_2C_2O_4$) were added into MO solutions to capture $^{\cdot}OH$ (hydroxyl radicals), $^{\cdot}O_2^-$ (superoxide radicals), electrons and holes, respectively. All solutions were kept under magnetic stirring in the UV spectral region, and further analyses were performed as described above.

3. RESULTS AND DISCUSSION

3.1. Structural, morphological, and physio-chemical characterization

Table 1 presents the theoretical and experimental chemical composition of the obtained samples. The theoretical composition was evaluated from the content of precursors in the reaction mixture, whereas an experimental one

Table 1 | Chemical composition of the as-obtained photocatalysts (wt.%)

	Theoretical		Experimental		
Sample	Bi_2O_3	SiO_2	Bi_2O_3	SiO_2	Na_2O
10-Bi-Si	10	90	22.0	75.3	2.7
25-Bi-Si	25	75	31.7	66.9	1.5
40-Bi-Si	40	60	59.1	35.6	0.1
50-Bi-Si	50	50	65.4	29.9	4.6
60-Bi-Si	60	40	42.9	16.4	40.6

was determined from the EDXRF results followed by recalculation for oxides. The measured content of bismuth oxide in the as-obtained samples is higher than that of the theoretical one, apparently due to an incomplete transition of sodium orthosilicate to silicic acid sol with a change in solution pH. The samples contain sodium because gelation was carried out in an alkaline medium, which was created by sodium hydroxide. It should be noted that 60-Bi-Si contains a high amount of sodium since a large dosage of $Bi(NO_3)_3$ requires additional amounts of NaOH solution to be added into the mixture in order to adjust the pH of the medium to 6.

Table 2 shows the results of the EDX analysis of surface layers (approximately 1 μm) for the studied catalysts. It can be seen that bismuth content rises at the surface with an increase in the amount of its oxide added into the samples (from 10 to 50%). The 60-Bi-Si sample has a low content of bismuth (6%) and a rather high content of sodium on the surface. Thus, excess sodium hydroxide in the solution leads to the formation of the sample with low bismuth content and high sodium content both in volume and on its surface. In this case, sol–gel transition does not occur and mixed composite structures are not formed. In addition, silicon content on the surface of 50-Bi-Si and 60-Bi-Si is quite low, which is also due to the peculiarities of the gelation process.

Table 2 | Average elemental composition of the as-obtained samples determined by EDX analysis

	Elemental composition (at.%)			
Sample	**O**	**Na**	**Si**	**Bi**
10-Bi-Si	65.7	1.9	29.6	2.9
25-Bi-Si	69.8	0.7	25.7	3.8
40-Bi-Si	66.6	1.7	21.8	9.8
50-Bi-Si	72.1	1.8	5.0	21.1
60-Bi-Si	64.7	22.2	6.7	6.4

Fig. 1S shows the Fourier transform infrared (FT-IR) result for the studied photocatalysts. FT-IR spectra of 10-Bi-Si and 25-Bi-Si samples are identical (Fig. 1Sa). In the FT-IR spectra, absorption bands correspond to bending (469 cm^{-1}) and stretching (symmetric and asymmetric) bands (804 and 1,099 cm^{-1}) of Si–O–Si siloxane bonds (Plyusnina 1976). With a higher content of bismuth oxide in the samples 40-Bi-Si (59.1%, Table 1), 50-Bi-Si (65.4%, Table 1), and 60-Bi-Si (42.9%, Table 1) (Figs. 1Sb and 1Sc), absorption bands appear at 1,385 and 619 cm^{-1}, specific to the Bi–O bond at 850 cm^{-1}, corresponding to Bi–O–Si vibrations (Dou *et al.* 2020a). In the samples 10-Bi-Si and 25-Bi-Si, the content of bismuth oxide is 22 and 31.7% (Table 1), respectively. The sample 40-Bi-Si contains 59.1% bismuth oxide and 50-Bi-Si contains 65.4% bismuth oxide (Table 1). It can be noted that FT-IR spectra of the 60-Bi-Si sample contain absorption bands at 1,640 and 3,450 cm^{-1}, indicating the presence of OH groups, which are caused by the presence of sorbed water (Fig. 1S).

According to XRD data (Table 3; Figs. 2S and 3S), 10-Bi-Si and 25-Bi-Si samples are in an amorphous–crystalline state, while 40-Bi-Si, 50-Bi-Si, and 60-Bi-Si are in a crystalline state. A diffuse peak corresponding to an amorphous structure is observed near $2\theta \approx 20°$ on XRD patterns of 10-Bi-Si and 25-Bi-Si samples. The samples contain cristobalite and 60-Bi-Si is a moganite. Crystallization of silica is due to a high sodium content. Bismuth silicate Bi_2SiO_5, which exhibits the highest photocatalytic activity among binary Bi_2O_3–SiO_2 systems, was formed in all the samples (Chen *et al.* 2017). 10-Bi-Si and 50-Bi-Si samples also contain photoactive cubic modification

Table 3 | Phase composition of the as-obtained photocatalysts

Sample	**Phase state**	**XRD data**
10-Bi-Si	Amorphous–crystalline	δ-Bi_2O_3, Bi_2SiO_5 (tetragonal), SiO_2 (cristobalite)
25-Bi-Si	Amorphous–crystalline	Bi_2SiO_5 (tetragonal), Bi_2SiO_5 (orthorhombic)
40-Bi-Si	Crystalline	$Bi_{12}SiO_{20}$ (tetragonal), Bi_2SiO_5 (orthorhombic)
50-Bi-Si	Crystalline	δ-Bi_2O_3, Bi_2SiO_5 (orthorhombic), SiO_2 (cristobalite)
50-Bi-Si*	Crystalline	δ-Bi_2O_3, Bi_2SiO_5 (orthorhombic), SiO_2 (cristobalite)
60-Bi-Si	Crystalline	$Bi_{12}SiO_{20}$ (tetragonal), Bi_2SiO_5 (orthorhombic), SiO_2 (moganite)

δ-Bi_2O_3. δ-Bi_2O_3 is one of the best-known oxygen ion conductors. The reason for extraordinarily high oxygen mobility in δ-Bi_2O_3 is more oxygen vacancies in the δ-phase naturally possesses (Dreyer *et al.* 2016).

XPS spectra were further carried out to confirm the chemical state of the elements in the samples. Figure 1(a) shows the survey spectra of the 50-Bi-Si sample. The major peaks correspond to electronic states of Bi 4f, Bi 4d, O 1s, Si 2p, and Na 1s.

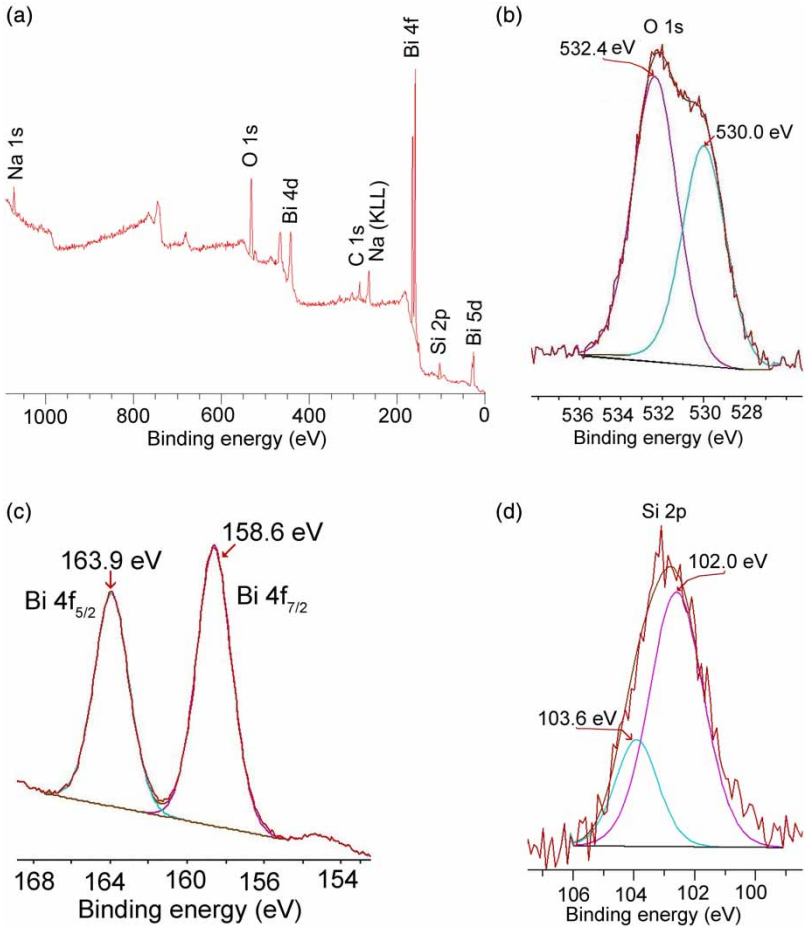

Figure 1 | XPS spectrum of 50-Bi-Si: the XPS survey spectrum (a), O 1s (b), Bi 4f (c), and Si 2p (d).

Figure 1(b) shows a high-resolution XPS peak of O 1s. The O 1s spectrum can be deconvoluted into two peaks. The peak at 532.4 eV is connected with the O 1s orbital of lattice oxygen of SiO_2 (Miller & Linton 1985), while the peak at 530.0 eV is the characteristic of oxygen of the Bi–O bond (Chen *et al.* 2017; Lu *et al.* 2018). As demonstrated in Figure 1(c), the binding energies at 158.6 and 163.9 eV can be ascribed to Bi 4f7/2 and Bi 4f5/2, respectively. These values of binding energies might belong to Bi^{3+} in both Bi_2SiO_5 and Bi_2O_3 (Lu *et al.* 2018; Dou *et al.* 2020a).

Figure 1(d) depicts the Si 2p XP spectra; the binding energies of 103.6 and 102.0 eV are attributed to Si(IV) of SiO_2 (Xu *et al.* 2013) and Bi_2SiO_5 (Chen *et al.* 2017), respectively.

Figure 2(a), 2(c), 2(e), 2(g), and 2(i) illustrate SEM images of the as-obtained materials. In all cases, particles were larger than 100 μm and their surface was inhomogeneous. The difference in the surface structure can be seen at a higher resolution (Figure 2(b), 2(d), 2(f), 2(h), and 2(j)). Samples with a small proportion of bismuth oxide (10-Bi-Si, 25-Bi-Si) have a spongy structure. It was formed during the interaction of biogenic silica and $Bi(NO_3)_3$, followed by washing and the removal of reaction products during calcination (Figure 2(b) and 2(d)). An increase in the content of bismuth oxide (40-Bi-Si and 50-Bi-Si; Table 1) led to a change in the surface morphology of powders (Figure 2(f) and 2(h)). The surface of these samples melted more, with granules of various shapes, which became coarser due to the increasing proportion of Bi_2O_3 in the samples. Multiple large crystals were found on the surface of the 60-Bi-Si sample (Figure 2(j)).

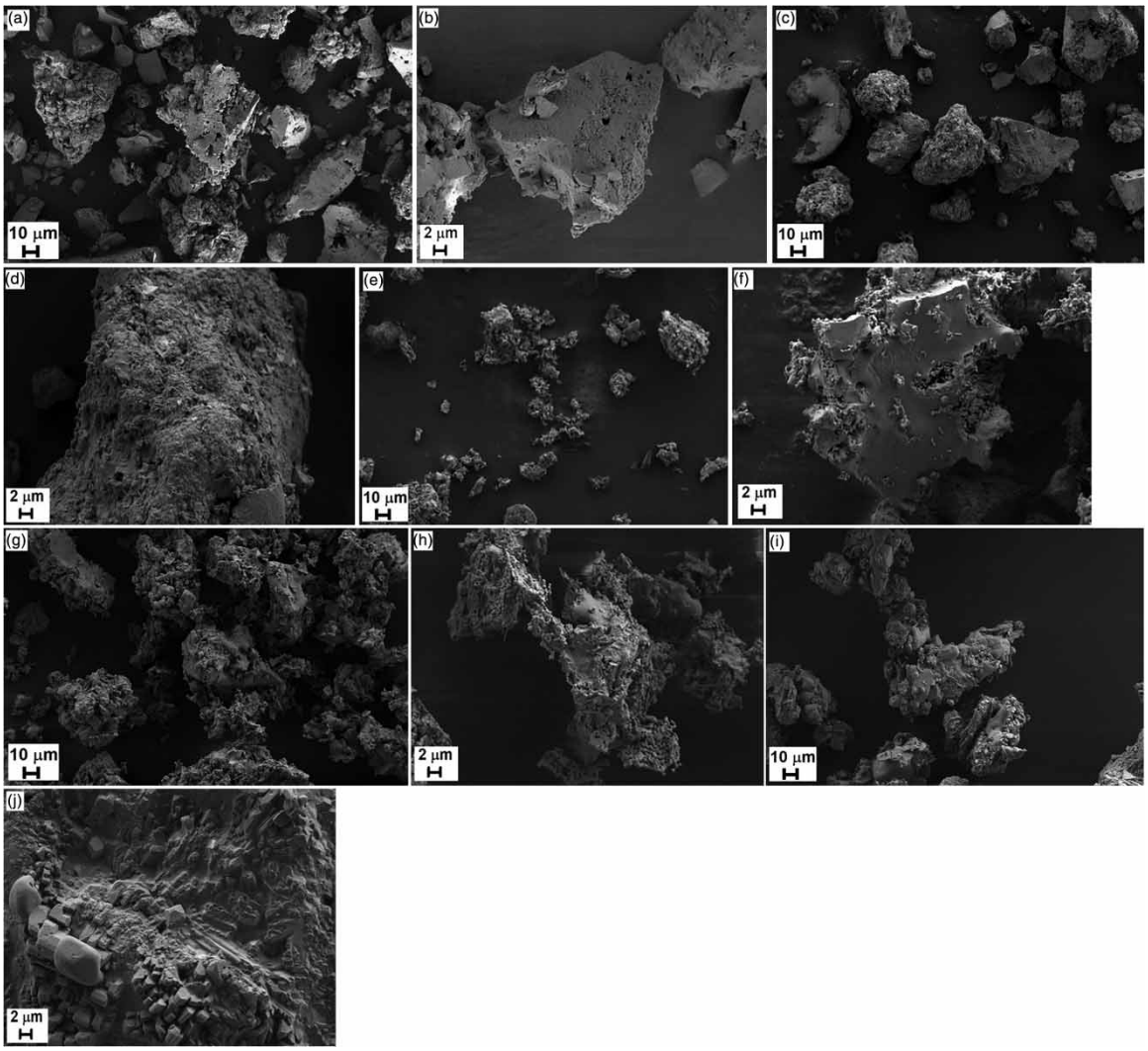

Figure 2 | SEM images of the as-obtained photocatalysts: (a, b) 10-Bi-Si; (c, d) 25-Bi-Si; (e, f) 40-Bi-Si; (g, h) 50-Bi-Si; (i, j) 60-Bi-Si.

An important characteristic of photocatalysts is a ZCP. The value of ZCP for Bi_2O_3 was in the neutral region (pH_{pzc} 6.9). The ZCP of the photocatalyst samples shifted to the alkaline side (from 9.60 for 10-Bi-Si to 10.85 for 60-Bi-Si (Figure 3)) in the presence of SiO_2 in the samples.

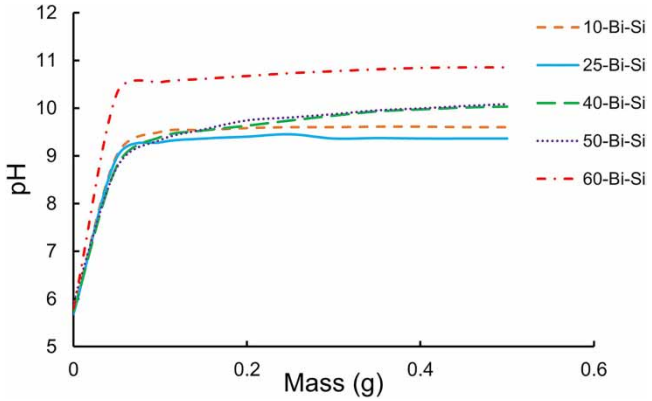

Figure 3 | pH variation in the aqueous suspension of the as-obtained photocatalysts.

3.2. Photodegradation of MO

The photocatalytic activity of the samples was evaluated in the degradation reaction of an organic pollutant (MO) under UV-light irradiation. At the same time, experiments were carried out without catalysts, which showed that regardless of the irradiation method, the dye decomposition did not occur. Results of photocatalytic tests during irradiation of the samples with UV light are shown in Figure 4. It can be seen that in the presence of SiO_2 (non-modified biogenic silica), Bi_2O_3 samples, and 10-Bi-Si and 25-Bi-Si products, MO degradation almost did not occur. An increase in Bi_2O_3 content in the samples up to 59% (sample 40-Bi-Si, Table 1) led to a manifestation of catalytic activity and the MO degradation degree reached 22%. χ values for the 50-Bi-Si sample (mass content of Bi_2O_3 65%, Table 1) were 45%. Catalytic activity did not manifest itself with a further increase in the theoretical content of Bi_2O_3 in the composite (60-Bi-Si sample).

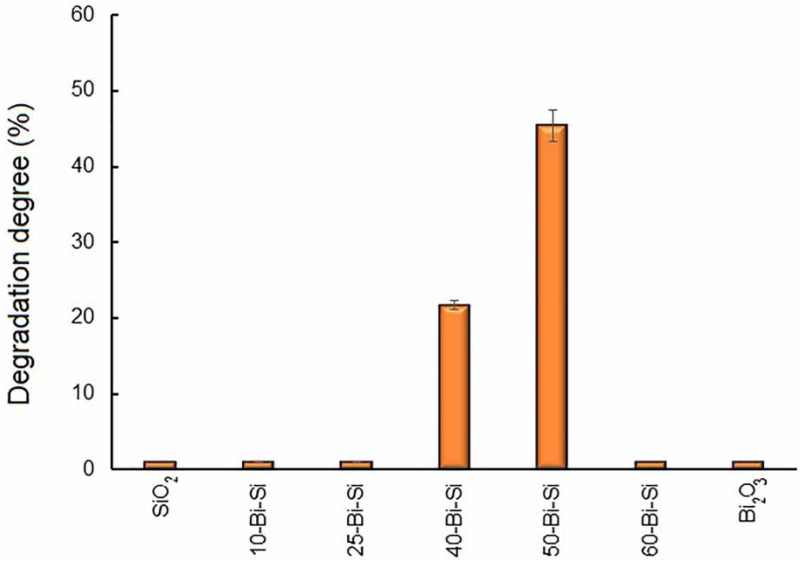

Figure 4 | MO degradation degree in the presence of the as-obtained photocatalysts in exposure to UV light.

It is known that the initial stage of heterogeneous catalytic processes is the sorption of substances on the surface of a solid. Solution pH has a crucial effect on the adsorption capacity of dyes. A change in the solution pH can modify the surface charge of an adsorbent and a dye ionization degree. According to the results shown in Figure 3, the pH_{pzc} of the photocatalysts was specified to be more than 7. It means that in the studied MO solution (pH 6.8), the surface is positively charged. MO is an anionic dye and can maintain its anionic configuration in the pH range of 3–14 (pKa = 3.8). This contributed to an interaction of the positive surface of all the studied samples with anionic dye (Rekavandi *et al.* 2019; Khan *et al.* 2022).

The low photocatalytic activity of 10-Bi-Si and 25-Bi-Si materials can be explained by their amorphous state (Table 3, Fig. 2S) and a high proportion of silicon dioxide (75 and 67%, respectively, (Table 1)), which, as a typical dielectric, blocks the generation of electron-hole pairs. The appearance of photocatalytic activity in 40-Bi-Si and 50-Bi-Si samples is associated with their transition to crystalline state (Table 3; Figs. 2S and 3S) and the formation of crystals on the surface (Figure 2(f) and 2(h)). The higher photoactivity of the 50-Bi-Si sample compared to 40-Bi-Si is explained by the formation of a two-phase system: δ-Bi_2O_3 and Bi_2SiO_5. In this system, Bi_2SiO_5 is a typical n-type semiconductor, and δ-Bi_2O_3 is a p-type semiconductor. This contributes to the formation of the p–n heterostructure and, as a consequence, efficient separation of photogenerated holes and electrons (Lu *et al.* 2018). The 60-Bi-Si sample has an insignificant photocatalytic activity due to an undeveloped surface and a low bismuth content (Table 2, Figure 2(j)).

3.3. Optoelectronic properties of the photocatalysts

Under conditions of irradiation with visible light, all obtained samples are inactive. The reason for this is the optical properties of the samples. UV–Vis diffuse spectroscopy was applied to study the optoelectronic properties of the photocatalysts. As illustrated in Figure 5(a), the analyzed 50-Bi-Si product is characterized by a stepwise shape

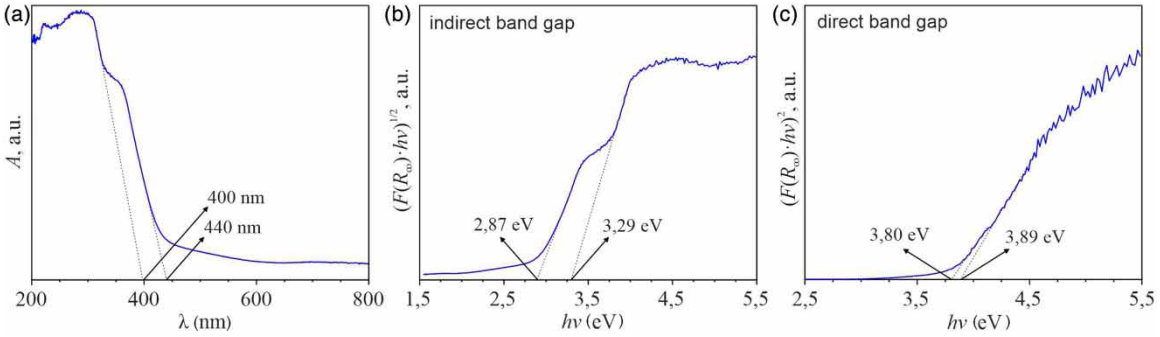

Figure 5 | UV–Vis DRS data for the 50-Bi-Si sample (a) and corresponding Tauc plots for indirect (b) and direct (c) electronic transitions represented in terms of the Kubelka–Munk theory.

of a spectral curve having two absorption edges, which originate from different kinds of electronic transitions. Intercepts on the *x*-axis found by tangents to a curve show that these absorption edges were around 400 and 440 nm corresponding to Bi_2SiO_5 and δ-Bi_2O_3, respectively. The effects are explained by the co-existence of different semiconducting compounds in the analyzed sample, which suggest that the formation of the binary heterophase system is based on δ-Bi_2O_3 and Bi_2SiO_5. With a further increase in wavelength, the studied 50-Bi-Si photocatalyst is inactive. Band gap energy (E_g) of 50-Bi-Si was calculated by the Tauc relation (Equation (4)), taking into account the Kubelka–Munk theory ($\alpha \sim F(R_\infty)$):

$$F(R_\infty)\cdot h\nu = B(h\nu - E_g)^n \tag{4}$$

where α is an absorption coefficient, B is a constant, and $h\nu$ – is a photon's energy, $F(R_\infty) = (1-R_\infty)^2/2R_\infty$ is the Kubelka–Munk function, R_∞ is a reflectivity, and n is a factor that is determined by the nature of the electronic transition between valence and conduction bands (equals to 1/2 or 2 for direct and indirect transitions).

The plots of $(F(R_\infty)\cdot h\nu)^{1/n}$ against $h\nu$ are shown in Figure 5(b) and 5(c). The analysis shows that these dependences are characterized by the presence of two linear segments, which correspond to different electronic levels allowing us to absorb photons. The E_g values are 2.87 eV ($n=2$) and 3.80 eV ($n=1/2$) for δ-Bi_2O_3 and 3.29 eV ($n=2$) and 3.89 eV ($n=1/2$) for Bi_2SiO_5. The obtained results are consistent with the reported values (Agasiev *et al.* 1986; Cheng *et al.* 2010; Dreyer *et al.* 2016; Gu *et al.* 2018).

3.4. E_{CB} and E_{VB} positions of δ-Bi_2O_3/Bi_2SiO_5 heterojunctions and photocatalytic enhancement mechanisms

A possible mechanism of analyzing electron-hole separation and transfer processes in the photocatalytic reaction was proposed for most active 50-Bi-Si photocatalysis-containing Bi_2SiO_5 and δ-Bi_2O_3 crystal phases. Figure 6 shows energy levels of Bi_2SiO_5, δ-Bi_2O_3, and Bi_2O_3/Bi_2SiO_5 heterojunction and a possible charge transfer process of heterojunctions under UV-light irradiation. Band positions of δ-Bi_2O_3 and Bi_2SiO_5 were calculated by the following empirical formulas:

$$E_{CB} = X - E_c - \frac{1}{2}E_g \tag{5}$$

$$E_{VB} = E_{CB} + E_g \tag{6}$$

where X is the absolute electronegativity of a semiconductor, expressed as a geometric mean of the absolute electronegativity of constituent atoms. This is defined as the arithmetic mean of atomic electron affinity and the first ionization energy; E_c is the energy of free electrons of hydrogen scale (4.5 eV); E_g is a semiconductor band gap; E_{CB} is a conduction band potential, and E_{VB} is a valence band potential.

From the plot of $(ahv)^2$–hv (Figure 5(c)), we estimated that band gaps of Bi_2SiO_5 and δ-Bi_2O_3 were 3.89 and 3.8 eV, respectively. X values for Bi_2SiO_5 and Bi_2O_3 were 6.12 and 5.91 eV, respectively. Valence band positions of δ-Bi_2O_3 and Bi_2SiO_5 were 3.31 and 3.56 eV, respectively. Conduction band positions of δ-Bi_2O_3 and Bi_2SiO_5 were −0.48 and −0.33 eV, respectively.

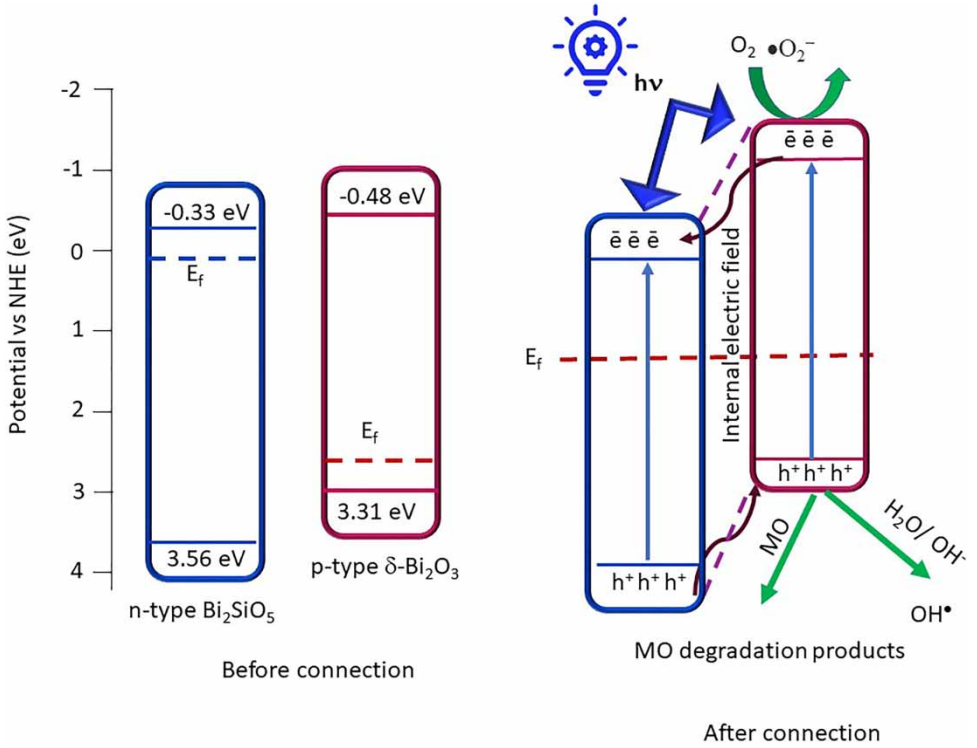

Figure 6 | Diagram for the energy level of δ-Bi_2O_3/Bi_2SiO_5 heterojunctions and the possible charge transfer process of the heterojunctions under UV irradiation.

When p-type δ-Bi_2O_3 and n-type Bi_2SiO_5 contacted each other, a p–n heterojunction was formed at an interface of a phase (Lu *et al.* 2018). In this process, energy levels of conduction (CB) and valence (VB) bands of p-type δ-Bi_2O_3 tended to ascend, while levels of n-type Bi_2SiO_5 tended to descend until a Fermi-level equilibrium was reached (Low *et al.* 2017). Because of the formation of the p–n heterojunction, a region close to the p–n interface was charged, creating an internal electric field (Low *et al.* 2017; Sun *et al.* 2017).

Under UV-light irradiation, both Bi_2SiO_5 and δ-Bi_2O_3 can absorb photons giving rise to electrons and holes. Because the CB of δ-Bi_2O_3 (−0.48 eV) is more negative than $O_2/^{\bullet}O_2^-$ potential (−0.33 eV vs. normal hydrogen electrode (NHE)), photogenerated electrons can react with O_2 to generate $^{\bullet}O_2^-$, which is an active species with strong oxidizing ability and can react with MO. Moreover, a high position of CB of δ-Bi_2O_3 and internal electric field at the interface lead to a transfer of photogenerated electrons from δ-Bi_2O_3 to Bi_2SiO_5. Meanwhile, photogenerated holes from a valence band of Bi_2SiO_5 can be easily transferred to a valence band of δ-Bi_2O_3 and then directly reacted with MO. Therefore, photogenerated holes and electrons can be separated effectively and photocatalytic activity is enhanced a lot.

Valence band positions of δ-Bi_2O_3 (3.31 eV) and Bi_2SiO_5 (3.56 eV) are more positive than those of $OH^{\bullet}/H_2O$ (2.27 eV) and $OH^{\bullet}/OH^-$ (1.99 eV) potentials before connection, indicating that $^{\bullet}OH$ can be generated by the oxidation reaction of h^+.

After the p–n heterojunction formation, E_{VB} of δ-Bi_2O_3 slightly reduced but its value remained favourable for a sufficient oxidation capability for $OH^{\bullet}/H_2O$ and $OH^{\bullet}/OH^-$ conversions. Therefore, MO can be degraded by the $O_2/^{\bullet}O_2^-$, h^+, or $OH^{\bullet}$ oxidation pathway.

3.5. Identification of reactive oxidative species in the photodegradation of MO

To disclose the photocatalytic mechanism of the as-obtained 50-Bi-Si photocatalyst, reaction rates were determined in the presence of reactive species ($^{\bullet}O_2^-$, h^+, e^-, or $^{\bullet}OH$) involved in the photocatalytic decomposition process. IPA, BQ, H_2O_2, and $(NH_4)_2C_2O_4$ were introduced as $^{\bullet}OH$, $^{\bullet}O_2^-$, electrons, and holes, respectively.

Usually, the kinetics of the photocatalytic degradation of organic pollutants is determined using the Langmuir–Hinshelwood model since it assumes that a degradation reaction occurs between generated reactive oxygen species and adsorbed pollutant molecules. As the second-order kinetic model typically fits the

Langmuir–Hinshelwood model, it can be simplified to a pseudo-first-order kinetic model by considering that the adsorbed amount of pollutant molecules is independent of its concentration in a medium (Mota *et al.* 2020).

Active species trapping experiment results for 50-Bi-Si are shown in Figure 7 and Table 2S. It is seen that all curves of $\ln(A_0/A)$ against time are almost linear, and the correlation coefficient (R^2) value is 0.7 (Figure 7, Table 2S). The value of R^2 in the range from 0.7 to 0.9 indicates that the model approximates the data well and indicates a fairly strong linear relationship. Calculated degradation rate constants for MO are given in Table 2S.

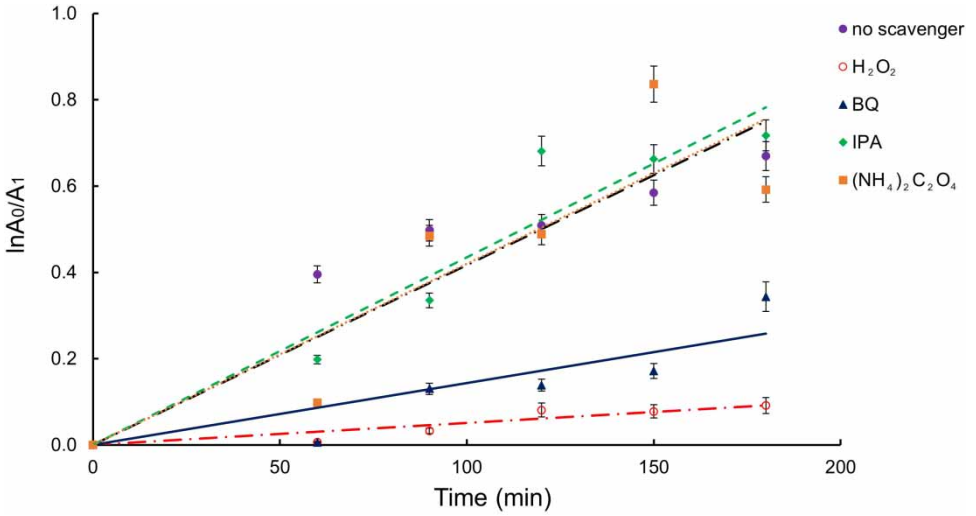

Figure 7 | Photodegradation of MO as a function of irradiation time for the 50-Bi-Si sample in the presence of reactive oxygen species.

As shown in Figure 7, $^{\bullet}O_2^-$ and e^- participate in a degradation process. Electrons play a dominant role, and $^{\bullet}O_2^-$ takes a second role since the rate constant of the MO degradation reaction in the presence of hydrogen peroxide is three times less (Table 2S). H^+ and $^{\bullet}OH$ do not play a role in the degradation process. Reaction rate constants in the presence of these scavengers do not differ from each other and the MO degradation constants in the absence of scavengers.

Equations (7)–(10) can represent the degradation process of MO with photogenerated reactive radicals:

$$Bi_2O_3/Bi_2SiO_5 + h \rightarrow h^+_{VB} + e^-_{CB} \quad (7)$$

$$e^-_{CB} + O_{2(ads)} \rightarrow O_2^{-\bullet} \quad (8)$$

$$O_2^{-\bullet} + H^+ \rightarrow HO_2^{\bullet} \quad (9)$$

$$MO + (^{\bullet}O_2^{-\bullet}/OOH^{\bullet}) \rightarrow \text{Degradation} \quad (10)$$

3.6. Photocatalyst stability

Photocatalyst stability is also an essential factor in practical application for a photocatalytic reaction. The authors of this paper used a time-circle MO photodegradation experiment to evaluate the stability of 50-Bi-Si photocatalyst. After each cycle, the catalyst was collected by centrifugation. As shown in Figure 8, MO degradation degree in the presence of the as-obtained photocatalyst 50-Bi-Si repeated and maintained its activity after the third cycle. *P*-criterion calculation was higher than 0.05 ($p = 0.8$), which meant that there was no statistical difference in the values of degradation efficiency of cycles 2 and 3. The used 50-Bi-Si was also examined by XRD. Fig. 2S shows XRD patterns of 50-Bi-Si before and after photodegradation. It is evident that the crystalline phase of 50-Bi-Si does not change after MO photodegradation.

The AAS method was used to determine bismuth concentration in aqueous solutions of MO after the third test cycle to assess the stability of the photocatalyst in aqueous solutions. Bismuth content in the MO solution after

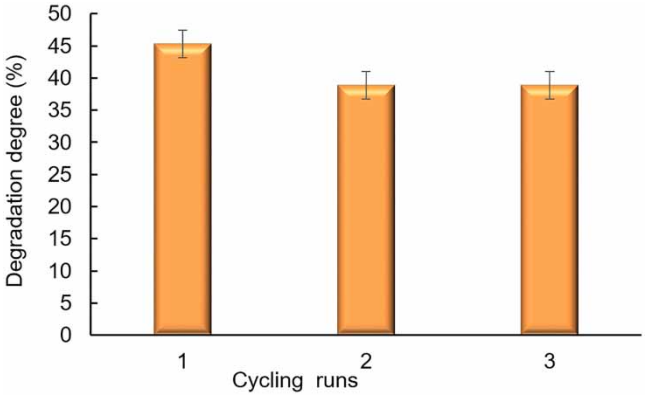

Figure 8 | Cycling runs in the photocatalytic degradation of MO in the presence of 50-Bi-Si.

each photocatalysis cycle did not exceed 0.2 mg L^{-1} (0.2 mg L^{-1} is the limit of detection of bismuth by the AAS method). Thus, the obtained results indicate that the studied catalysts are stable in aqueous solutions. The content of bismuth does not exceed 0.2 (0.2 is the limit of detection of bismuth)

4. CONCLUSIONS

Photocatalytically active δ-Bi_2O_3/Bi_2SiO_5 heterostructures were synthesized by the sol–gel method using bismuth nitrate and biogenic silica produced from rice husk. The influence of the content of bismuth oxide in the samples on their composition, structure and photocatalytic properties was shown.

It was established that the obtained samples contain photoactive Bi_2SiO_5 and, in some cases, δ-Bi_2O_3 and $Bi_{12}SiO_{20}$. The as-obtained samples exhibit photocatalytic activity in the oxidation of MO under UV irradiation. Extensive characterization revealed the relationship between the content of bismuth oxide in materials and their photocatalytic properties. A degree of UV-light-assisted degradation of MO degradation in a neutral medium (pH 6.8), in the presence of the samples containing 59–65% Bi_2O_3, reaches 22–45% in 60 min. Hence, enhanced photocatalytic performance can be ascribed to the formation of δ-Bi_2O_3 and, probably, the fabrication of δ-Bi_2O_3/Bi_2SiO_5 heterojunction. The as-obtained photocatalysts remain stable in aqueous solutions, and bismuth leaching after photocatalytic tests does not exceed 0.2 mg L^{-1}. This study evaluated the roles of different reactive oxygen species on the degradation kinetics of MO on Bi_2O_3/Bi_2SiO_5 using radical scavengers. It was found that electrons were the main active species for the degradation of MO by UV irradiation, whereas $^{\bullet}O_2^-$ played a supporting role during the photocatalytic process.

Thus, the heterostructures obtained by a simple sol–gel method using biogenic silica are environmentally acceptable, easily separated from the solution, and exhibit photocatalytic activity without acidification and the addition of oxidants. Based on the mentioned above, the as-obtained δ-Bi_2O_3/Bi_2SiO_5 samples are promising photocatalysts for water treatment from persistent organic pollutants in natural conditions.

ACKNOWLEDGEMENTS

This work was supported by the state task of the Institute of Chemistry of the FEB RAS FWFN(0205)-2022-0002 (topic 1, section 3); the UV–Vis studies were performed with the financial support of the Russian Science Foundation under Grant number 22-23-00912. The study of the morphology of the surface of the samples was carried out on the equipment of the Center for Collective Use of the Far Eastern Federal University No. 200556 (Vladivostok).

DATA AVAILABILITY STATEMENT

All relevant data are included in the paper or its Supplementary Information.

CONFLICT OF INTEREST

The authors declare there is no conflict.

REFERENCES

Adam, F. & Andas, J. 2007 Amino benzoic acid modified silica – An improved catalyst for the mono-substituted product in the benzylation of toluene with benzyl chloride. *Journal of Colloid and Interface Science* **311**, 135–143. https://doi.org/10.1016/j.jcis.2007.02.083.

Adam, F., Andas, J. & Rahman, I. A. 2010 A study on the oxidation of phenol by heterogeneous iron silica catalyst. *Chemical Engineering & Technology* **165**, 658–667. https://doi.org/10.1016/j.cej.2010.09.054.

Agasiev, A. A., Zeinally, A. K., Alekperov, S. J. & Guseinov Ya, Y. 1986 Photoelectrical properties of α-bi$_2$o$_3$ thin films. *Materials Research Bulletin* **21**, 765–771.

Arefieva, O. D., Vasilyeva, M. S., Kuryavy, V. G., Ustinov, A. Y., Zemnukhova, L. A. & Gushchi, D. D. 2020 Oxidative destruction of phenol on Fe/SiO_2 catalysts. *Water Science and Technology* **81**, 2189–2201. https://doi.org/10.2166/wst.2020.277.

Arefieva, O. D., Vasilyeva, M. S., Lukiyanchuk, I. V., Sedinkina, E. S., Zemnukhova, L. A. & Pisartseva, A. I. 2021a Preparation and photocatalytic properties of β-Bi_2O_3/Bi_2SiO_5 heterostructures. *Russian Journal of Inorganic Chemistry* **66**, 836–842. https://doi.org/10.1134/S0036023621060036.

Arefieva, O. D., Vasilyeva, M. S., Zemnukhova, L. A. & Timochkina, A. S. 2021b Heterogeneous photo-Fenton oxidation of lignin of rice husk alkaline hydrolysates using Fe-impregnated silica catalysts. *Environmental Technology* **42**, 2220–2228. https://doi.org/10.1080/09593330.2019.1697376.

Bailiche, Z., Cherif, L., Royer, S., Bengueddach, A., Fourmentin, S. & Siffert, S. 2013 Heterogeneous advanced photo-Fenton oxidation of phenolic aqueous solutions over iron-containing SBA-15 catalyst. *MATEC Web of Conferences* **040033**, 1–4. http://dx.doi.org/10.1051/matecconf/20130504033.

Chen, R., Bi, J., Wu, L., Wang, W., Zh, L. & Fu, X. 2009 Template-free hydrothermal synthesis and photocatalytic performances of novel Bi_2SiO_5 nanosheets. *Inorganic Chemistry* **48**, 9072–9076. https://doi.org/10.1021/ic901084s.

Chen, Y.-C., Liu, C.-P., Yang, C.-K., Huang, B.-Y. & Liu, C.-Y. 2013 Preparation and release properties of sol-gel encapsulated proteins. *Journal of Analytical Sciences, Methods and Instrumentation* **3**, 20–24. https://doi.org/10.4236/jasmi.2013.33A002.

Chen, C.-C., Yang, C.-T., Chung, W.-H., Chang, J.-L. & Lin, W.-Y. 2017 Synthesis and characterization of $Bi_4Si_3O_{12}$, Bi_2SiO_5, and $Bi_{12}SiO_{20}$ by controlled hydrothermal method and their photocatalytic activity. *Journal of the Taiwan Institute of Chemical Engineers* **78**, 157–167. http://dx.doi.org/10.1016/j.jtice.2017.05.021.

Cheng, H., Huang, B., Lu, J., Wang, Z., Xu, B., Qin, X., Zhang, X. & Dai, Y. 2010 Synergistic effect of crystal and electronic structures on the visible-light-driven photocatalytic performances of Bi_2O_3 polymorphs. *Physical Chemistry Chemical Physics* **12**, 15468–15475. https://doi.org/10.1039/C0CP01189D.

Cui, Z.-M., Hao, J., Liu, J. & Song &, W.-G. 2016 Mesoporous silica coating on hierarchical flowerlike Fe_2O_3 with enhanced catalytic activity for Fenton-like reaction. *RSC Advances* **6**, 74545–74549. https://doi.org/10.1039/C6RA15092F.

Dou, L., Jin, X., Chen, J., Zhong, J., Li, J., Zeng, Y. & Duan, R. 2020a One-pot solvothermal fabrication of S-scheme OVs-Bi_2O_3/Bi_2SiO_5 microsphere heterojunctions with enhanced photocatalytic performance toward decontamination of organic pollutants. *Applied Surface Science* **527**, 146775. https://doi.org/10.1016/j.apsusc.2020.146775.

Dou, L., Xiang, Y., Zhong, J., Li, J. & Huang, S. 2020b Ionic liquid-assisted preparation of thin Bi_2SiO_5 nanosheets for effective photocatalytic degradation of RhB. *Journal of Materials Chemistry A* **261**, 127117. https://doi.org/10.1016/j.matlet.2019.127117.

Dreyer, J. A. H., Pokhrel, S., Birkenstock, J., Hevia, M. G., Schowalter, M., Rosenauer, A., Urakawa, A., Yang Teoh, W. & Mädler, L. 2016 Decrease of the required dopant concentration for δ-Bi_2O_3 crystal stabilization through thermal quenching during single-step flame spray pyrolysis. *Royal Society of Chemistry* **18**(12), 2046–2056. https://doi.org/10.1039/c5ce02430g.

Espro, C., Marini, S. & Galvagno, S. 2016 Heterogeneous Fenton like catalysts for the selective oxidation of light alkanes in aqueous medium. *International Journal of Applied Chemistry* **12**, 713–726.

Fei, Y. T., Fan, S. J., Sun, R. Y., Xu, J. Y. & Ishii, M. 2000a Crystallizing behavior of Bi_2O_3-SiO_2 system. *Journal of Materials Science Letters* **19**, 893–895. https://doi.org/10.1023/A:1006701901976.

Fei, Y., Shiji, F., Renying, S. & Ishii, M. 2000b Study on phase diagram of Bi_2O_3-SiO_2 system for Bridgman growth of $Bi_4Si_3O_{12}$ single crystal. *Progress in Crystal Growth and Characterization of Materials* **40**, 183–188. https://doi.org/10.1016/S0960-8974(00)00003-6.

Gan, P. P. & Li, S. F. Y. 2013 Efficient removal of Rhodamine B using a rice hull-based silica supported iron catalyst by Fenton-like process. *Chemical Engineering & Technology* **229**, 351–363. https://doi.org/10.1016/j.cej.2013.06.020.

Ghime, D. & Ghosh, P. 2017 Heterogeneous Fenton degradation of oxalic acid by using silica supported iron catalysts prepared from raw rice husk. *Journal of Water Process Engineering* **19**, 156–163. https://doi.org/10.1016/j.jwpe.2017.07.025.

Gu, W., Teng, F., Liu, Z., Liu, Z., Yang, J. & Teng, Y. 2018 Synthesis and photocatalytic properties of Bi_2SiO_5 and $Bi_{12}SiO_{20}$. *Journal of Photochemistry and Photobiology A: Chemistry* **353**, 395–400. https://doi.org/10.1016/j.jphotochem.2017.11.047.

Hanna, K., Kone, T. & Medjahdi, G. 2008 Synthesis of the mixed oxides of iron and quartz and their catalytic activities for the Fenton-like oxidation. *Catalysis Communications* **9**, 955–959. https://doi.org/10.1016/j.catcom.2007.09.035.

Karthika, K., Sunaja Devia, K. R., Pinheiroa, D. & Sugunan, S. 2019 Photocatalytic activity of bismuth silicate heterostructures synthesized via surfactant mediated sol-gel method. *Materials Science in Semiconductor Processing* **102**, 1–8. https://doi.org/10.1016/j.mssp.2019.10458.

Khan, M. I., Shanableh, A., Elboughdiri, N., Lashari, M. H., Manzoor, S., Shahida, S., Farooq, N., Bouazzi, Y., Rejeb, S., Elleuch, Z., Kriaa, K. & Rehman, A. 2022 Adsorption of methyl orange from an aqueous solution onto a BPPO-based anion exchange membrane. *ACS Omega* **7**, 26788–26799. https://doi.org/10.1021/acsomega.2c03148.

Liu, D., Wang, J., Zhang, M., Liu, Y. & Zhu, Y. 2014 A superior photocatalytic performance of a novel Bi_2SiO_5 flower-like microsphere via a phase junction. *Nanoscale* **6**, 15222–15227. https://doi.org/10.1039/C4NR05058D.

Low, J., Yu, J., Jaroniec, M., Wageh, S. & Al-Ghamdi, A. A. 2017 Heterojunction photocatalysts. *Advanced Materials* **29**(20), 1601694. https://doi.org/10.1002/adma.201601694.

Lu, H., Hao, Q., Chen, T., Zhang, L., Chen, D., Ch, M., Yao, W. & Zhu, Y. 2018 A high-performance Bi_2O_3/Bi_2SiO_5 p-n heterojunction photocatalyst induced by phase transition of Bi_2O_3. *Applied Catalysis B* **237**, 59–67. https://doi.org/10.1016/j.apcatb.2018.05.069.

Miller, M. L. & Linton, R. W. 1985 X-ray photoelectron spectroscopy of thermally treated silica (SiO_2) surfaces. *Analytical Chemistry* **57**(12), 2314–2319. https://doi.org/10.1021/ac00289a033.

Mota, H. P., Quadrado, R. F. N., Iglesias, B. A. & Fajardo, A. R. 2020 Enhanced photocatalytic degradation of organic pollutants mediated by Zn (II)-porphyrin/poly(acrylic acid) hybrid microparticles. *Applied Catalysis B: Environmental* **277**, 119208. https://doi.org/10.1016/j.apcatb.2020.119208.

Noh, J. S. & Schwarz, J. A. 1989 Estimation of the point of zero charge of simple oxides by mass titration. *Journal of Colloid and Interface Science* **130**(1), 157–164. https://doi.org/10.1016/0021-9797(89)90086-6).

Onderka, B., Fitzner, K., Kopyto, M. & Przybyło, W. 2017 Thermodynamics of Bi_2O_3–SiO_2 system. *Journal of Mining and Metallurgy, Section B* **53**, 223–231. https://doi.org/10.2298/JMMB170701035O.

Plyusnina, I. I. 1976 *Infrared Spectra of Minerals*. Moscow Publishing House. Un-ta, Moscow, p. 175.

Pode, R. B. 2016 Potential applications of rice husk ash waste from rice husk biomass power plant. *Renewable and Sustainable Energy Reviews* **53**, 1468–1485. https://doi.org/10.1016/j.rser.2015.09.051.

Rekavandi, N., Malekzadeh, A. & Ghiasi, E. 2019 Methyl orange degradation using nano-$LaMnO_3$ as a green catalyst under the mild conditions. *Nanochemistry Research* **4**(1), 1–10. https://doi.org/10.22036/ncr.2019.01.001.

Sun, J., Li, X., Zhao, Q., Tadé, M. O. & Liu, S. 2017 Construction of p-n heterojunction β-$Bi_2O_3/BiVO_4$ nanocomposite with improved photoinduced charge transfer property and enhanced activity in degradation of ortho-dichlorobenzene. *Applied Catalysis B: Environmental* **219**, 259–268. https://doi.org/10.1016/j.apcatb.2017.07.052.

Tyulyagin 2022 Ranking of the World's Leading Countries in Rice Production, Consumption, Export and Import Tyulyagin: About the Economy, Investments, Technologies and the Future. Available from: https://tyulyagin.ru/ratings/rejting-stran-liderov-mira-po-proizvodstvu-risa.html (accessed 08 April 2022).

Takamori, T. 1990 The system Bi_2O_3-SiO_2. *Journal of the American Ceramic Society* **73**, 158–160. https://doi.org/10.1111/j.1151-2916.1990.tb05112.x.

Wei, W., Xie, J., Meng, S., Lu, X., Yan, Z., Zhu, J. & Cui, H. 2013 Synthetic bismuth silicate nanostructures: Photocatalysts grown from silica aerogels precursors. *Journal of Materials Research* **28**, 1658–1668. https://doi.org/10.1557/jmr.2013.65.

Wu, Y., Li, M., Wang, X., Wang, L. & Gao, H. 2017 Preparation and fluorescence property of pure Bi_2SiO_5 powders by Pechini sol-gel method. *Materials and Manufacturing Processes* **32**(5), 480–483. https://doi.org/10.1080/10426914.2016.1221081.

Xu, Z., Yu, J. & Xiao, W. 2013 Microemulsion-assisted preparation of a mesoporous ferrihydrite/SiO_2 composite for the efficient removal of formaldehyde from air. *Chemistry: A European Journal* **19**(29), 9592–9598. https://doi.org/10.1002/chem.201300438.

Zemnukhova, L. A., Egorov, A. G., Fedorishcheva, G. A., Sokol'nitskaya, T. A., Barinov, N. N. & Botsul, A. I. 2006 Properties of amorphous silica produced from rice and oat processing waste. *Inorganic Materials* **42**(1), 24–29. https://doi.org/10.1134/S0020168506010067.

Zhang, L., Wang, W., Sun, S., Xu, J., Shang, M. & Ren, J. 2010 Hybrid Bi_2SiO_5 mesoporous microspheres with light response for environment decontamination. *Applied Catalysis B* **100**, 97–101. https://doi.org 10.1016/j.apcatb.2010.07.018.

Zhong, X., Royer, S., Zhang, H., Huang, Q., Valange, S., Barrault, J. & Xiang, L. 2011 Mesoporous silica iron-doped as stable and efficient heterogeneous catalyst for the degradation of C.I. Acid Orange 7 using sono–photo-Fenton process. *Separation and Purification Technology* **80**, 163–171. https://doi.org/10.1016/j.seppur.2011.04.024.

First received 2 August 2023; accepted in revised form 20 June 2024. Available online 16 July 2024